Pergamon

PII: S0022-4073(98)00017-X

J. Quant. Spectrosc. Radiat. Transfer Vol. 60, No. 3, pp. 425–438, 1998

Printed in Great Britain
0022–4073/98 $19.00 + 0.00

RADIATION PRESSURE CROSS SECTION FOR FLUFFY AGGREGATES

HIROSHI KIMURA† and INGRID MANN

Max-Planck-Institut für Aeronomie, Max-Planck-Straße 2, D-37191 Katlenburg-Lindau, Germany

Abstract—We apply the discrete dipole approximation (DDA) to estimate the radiation pressure cross section for fluffy aggregates by computing the asymmetry parameter and the cross sections for extinction and scattering. The ballistic particle–cluster aggregate and the ballistic cluster–cluster aggregate consisting of either dielectric or absorbing material are considered to represent naturally existing aggregates. We show that the asymmetry parameter perpendicular to the direction of wave propagation is maximized where the wavelength is comparable to the aggregate size, which may be characterized by the area-equivalent radius or the radius of gyration rather than the volume-equivalent radius. The asymmetry parameter for the aggregate depends on the morphology of the particle, but not on the constituent material. Therefore, the dependence of the radiation pressure cross section on the material composition arises mainly from that of the extinction and scattering cross sections, in other words, the single-scattering albedo. We find that aggregates consisting of high-albedo material show a large deviation of radiation pressure from the direction of incident radiation. When the aggregates are illuminated by blackbody radiation, the deviation of the radiation pressure increases with increasing temperature of the blackbody.

Since the parallel component of the radiation pressure cross section for the aggregates is smaller than that for the volume-equivalent spheres at the size parameter close to unity, the Planck-mean radiation pressure cross section for the aggregates having radius comparable to the effective wavelength of radiation shows a lower value, compared with the volume-equivalent sphere. Consequently, the slope of the radiation pressure force per mass of the particle as a function of particle mass shows a lower maximum for the aggregates than for compact spherical particles.

1. INTRODUCTION

The radiation pressure force acting on a particle is essential in any discussion of the dynamics of a particle illuminated by light. In particular radiation pressure on cosmic dust has been regarded as an important topic of astrophysical interest, because a great number of subjects are related to the estimation of radiation pressure on cosmic dust, i.e., orbital evolution of cometary and asteroidal dust,[1] the lifetime of circumstellar dust for fall into a star due to Poynting–Robertson effect or for radiative blowoff,[2–4] the formation of the solar dust ring,[5] the penetration distance of interstellar dust into the solar system,[6] and the erosion of outer dust cloud around Vega-type stars.[7,8]

The radiation pressure arises from the momentum transfer of incident light on a particle due to the absorption and scattering process, since the electromagnetic wave carries momentum as well as energy. A quantitative estimation of radiation pressure is obtained by the calculation of the radiation pressure cross section, which is usually weighted with the spectrum of the incident light. The radiation pressure cross section is determined by the scattering asymmetry parameter and the cross sections for extinction and scattering. The asymmetry parameter and the cross sections are also important parameters to obtain the optical properties of atmospheres, such as Titan's atmosphere[9] and dust shells around Herbig Ae/Be stars.[10] Apparently, a theory of light scattering by particles is required to estimate the asymmetry parameter and the cross sections and hence the radiation pressure force.

† Author to whom correspondence sould be addressed.

The Rayleigh approximation or geometrical optics may be applicable to the calculation of the optical properties, i.e., the asymmetry parameter and the cross sections for particles considerably smaller or larger compared with the wavelength of incident light. When the size of the particle is comparable with the wavelength of incident radiation, Maxwell's equations must be solved directly, taking into account the morphology of the particles, because the optical properties depend on the shape and structure of the particle.

If a particle is assumed to be a homogeneous compact sphere, then the optical properties of the particle are calculated by Mie theory,[11,12] which is the exact solution of Maxwell's equations for a sphere. Clearly, the incident wave on the spherical particle is scattered symmetrically with respect to the direction of the wave propagation. As a result, the radiation pressure force acts on the particle along the direction of incident radiation. An ensemble of randomly oriented identical particles reacts in the same manner, even if the particles are non-spherical.[11] Therefore, the T-matrix method developed by Waterman[13,14] can be applied to compute the radiation pressure cross section for randomly oriented non-spherical particles.[15]

In contrast, the light scattered by individual non-spherical particles shows an asymmetry with respect to the direction of the incoming radiation. As a result, non-spherical particles have a component of radiation pressure perpendicular to the direction of the incident wave. The method of separation of variables[16] has been used to investigate the parallel and perpendicular components of radiation pressure force acting on axially symmetric non-spherical particles, such as infinite cylinders[17,18] and spheroids.[19–21] However, natural small particles, such as soot particles,[22] atmospheric aerosols[23] and cosmic dust[24–26] are neither homogeneous spheres, infinite cylinders, nor spheroids, but are often of irregular shape and appear in rather fluffy aggregates if the particles were formed by coagulation.[27,28] Regarding fluffy aggregates as hypothetical porous spheres, Mie theory has been applied to estimate the orientational average of the radiation pressure acting on the aggregates using the refractive index derived by effective medium theory.[5,29,30] Nevertheless, the Mie theory combined with the effective medium theory does not lead to a correct understanding of the perpendicular component of the radiation pressure acting on fluffy aggregates. Among the available techniques for solving Maxwell's equations, the discrete dipole approximation (DDA) established by Purcell and Pennypacker,[31] most easily handles the evaluation of the optical properties of aggregates.[32–42] We are therefore convinced that numerical results obtained by the DDA are helpful in extending our knowledge of radiation pressure acting on naturally existing aggregates.

2. DISCRETE DIPOLE APPROXIMATION

2.1. *Method of solution*

In the DDA, a particle is divided by N interacting dipoles, and a self-consistent set of complex dipole moments $\boldsymbol{P}_j$ ($j = 1, \ldots, N$) for the dipoles is obtained by solving $3N$ complex linear equations. It has been proved that complex-conjugate gradient (CCG) method for finding the $\boldsymbol{P}_j$ iteratively is effective and efficient.[43] When dipoles are located on a periodic lattice, such as a cubic lattice, the CCG method is usually combined with the fast-Fourier-transform (FFT) method, which accelerate the computations most efficiently.[44] It should, however, be mentioned that the FFT method may lose the advantage for highly porous particles. Because we treat fluffy aggregates and furthermore do not restrict the configuration of dipoles on any periodic lattice, the DDA is performed without application of the FFT method in this study. Note that the dipole polarizabilities α_j and the configuration of the dipoles are important input parameters in the DDA.

2.2. *Cross sections for extinction, absorption and scattering*

Once the dipole moments $\boldsymbol{P}_j$ are obtained by the CCG method within a specified level of accuracy, the extinction and absorption cross sections are evaluated by the optical theorem.[43] Then the scattering cross section C_{sca} can be derived from the subtraction of the absorption cross section C_{abs} from the extinction cross section C_{ext}. It is worthwhile noting that if absorption dominates extinction, then higher accuracy is required for computing C_{ext} and C_{abs} to determine C_{sca} from the subtraction. This means that the subtraction results in lower accuracy for evaluating the scattering

cross section for the aggregates having low albedo, which is defined by the ratio of scattering to extinction cross sections C_{sca}/C_{ext}. Therefore, it is reasonable to use the subtraction for the determination of C_{sca} only when $C_{sca}/C_{ext} \gg 0.01$.

Alternatively, the scattering cross section C_{sca} can be evaluated by the integration of the differential scattering cross section over the solid angle[43] and this method could be applied to evaluate C_{sca} with a reasonable accuracy when $C_{sca}/C_{ext} \ll 0.01$. In practical computation, we determine the scattering cross section C_{sca} by

$$C_{sca} = \frac{C_{sca}^{(0)} + (C_{ext} - C_{abs}) f_a^2}{1 + f_a^2}, \tag{1}$$

where $C_{sca}^{(0)}$ denotes the scattering cross section obtained by the integration of the differential scattering cross section and

$$f_a = 100 \frac{C_{sca}^{(0)}}{C_{ext}}. \tag{2}$$

Equation (1) is used to smoothly interpolate the extreme cases discussed above.

2.3. Asymmetry parameter

If the shape of a particle is symmetric with respect to the wave vector of the incident light, then the scattering asymmetry of light appears only in the direction of wave propagation. However, the scattering asymmetry of non-spherical particles apparently deviates from the direction of wave propagation. In order to generalize the asymmetry parameter for arbitrary shaped particles, we define the asymmetry parameter by

$$\boldsymbol{g} = \frac{1}{C_{sca}} \int \hat{\boldsymbol{n}} \frac{\mathrm{d}C_{sca}}{\mathrm{d}\chi} \mathrm{d}\chi, \tag{3}$$

where $\mathrm{d}\chi$ is the element of solid angle in the direction $\hat{\boldsymbol{n}}$ of scattering and $\mathrm{d}C_{sca}/\mathrm{d}\chi$ is the differential scattering cross section. The asymmetry parameter $\boldsymbol{g}$ can be interpreted as the mean direction of scattered light. If we introduce a Cartesian coordinate system, in which the unit vectors $\hat{\boldsymbol{e}}_1$, $\hat{\boldsymbol{e}}_2$, and $\hat{\boldsymbol{e}}_3$ are orthogonal and $\hat{\boldsymbol{e}}_1$ is parallel to the wave vector $\boldsymbol{k}$, the usual asymmetry parameter for a spherical particle is expressed as $\boldsymbol{g} \cdot \hat{\boldsymbol{e}}_1$.

Once the polarizations $\boldsymbol{P}_j$ at position $\boldsymbol{r}_j$ of jth dipole are known for the incident plane wave $\boldsymbol{E}_{inc,j} = \boldsymbol{E}_0 \exp(\mathrm{i}\boldsymbol{k} \cdot \boldsymbol{r}_j - \mathrm{i}\omega t)$, the asymmetry parameter $\boldsymbol{g}$ is calculated by

$$g_i = \frac{k^4}{C_{sca}|\boldsymbol{E}_0|^2} \int \hat{\boldsymbol{n}} \cdot \hat{\boldsymbol{e}}_i \left| \sum_{j=1}^{N} [\boldsymbol{P}_j - \hat{\boldsymbol{n}}(\hat{\boldsymbol{n}} \cdot \boldsymbol{P}_j)] \, \mathrm{e}^{-\mathrm{i}k\hat{\boldsymbol{n}} \cdot \boldsymbol{r}_j} \right|^2 \mathrm{d}\chi. \tag{4}$$

where $\boldsymbol{g} = g_1\hat{\boldsymbol{e}}_1 + g_2\hat{\boldsymbol{e}}_2 + g_3\hat{\boldsymbol{e}}_3$; $|\boldsymbol{k}| = k = \omega/c$ is the wave number. In this paper, numerical integrations are performed by Romberg's method to decrease cpu time and adjust the accuracy.[45]

2.4. Radiation pressure cross section

The momentum removed from the direction of wave propagation per unit time is obtained by $UC_{ext}\hat{\boldsymbol{e}}_1$, where U is the energy density of incident radiation. On the other hand, the scattered radiation carries off momentum and exerts a reaction force on the particle that is expressed as $-UC_{sca}\boldsymbol{g}$. Accordingly, the rate of momentum transfer on the particle is given by $U(C_{ext}\hat{\boldsymbol{e}}_1 - C_{sca}\boldsymbol{g})$, which is called the radiation pressure. Note that the radiation pressure is no longer parallel to the direction $\boldsymbol{k}$, unless $g_2 = g_3 = 0$. Therefore, we define the radiation pressure cross section $C_{pr,i}$ $(i = 1, 2, 3)$ by $C_{ext}\hat{\boldsymbol{e}}_1 - C_{sca}\boldsymbol{g} = C_{pr,1}\hat{\boldsymbol{e}}_1 + C_{pr,2}\hat{\boldsymbol{e}}_2 + C_{pr,3}\hat{\boldsymbol{e}}_3$. This yields

$$C_{pr,1} = C_{ext} - C_{sca}g_1, \tag{5}$$

$$C_{pr,2} = -C_{sca}g_2, \tag{6}$$

$$C_{pr,3} = -C_{sca}g_3, \tag{7}$$

where $C_{pr,1}$ is the usual cross section of radiation pressure, which has been applied for homogeneous spheres.[12]

2.5. Planck-mean radiation pressure cross section

We use the Planck function of blackbody radiation as a spectrum of incident light. The radiation pressure force $\boldsymbol{F}_{\mathrm{R}}$ acting on the particle exposed to the blackbody radiation is expressed as

$$\boldsymbol{F}_{\mathrm{R}} = \left(\frac{\sigma T^4}{c}\right)\left(\frac{\Omega}{\pi}\right)(\langle C_{\mathrm{pr},1}\rangle \hat{\boldsymbol{e}}_1 + \langle C_{\mathrm{pr},2}\rangle \hat{\boldsymbol{e}}_2 + \langle C_{\mathrm{pr},3}\rangle \hat{\boldsymbol{e}}_3), \tag{8}$$

where σ is Stefan–Boltzmann constant, T is the blackbody temperature of the radiation source, and Ω is the solid angle subtended by the blackbody. The mean cross section of radiation pressure $\langle C_{\mathrm{pr},i}\rangle$ $(i = 1, 2, 3)$ weighted by the Planck function is defined by

$$\langle C_{\mathrm{pr},i}\rangle = \frac{\pi}{\sigma T^4}\int_0^\infty B_\lambda C_{\mathrm{pr},i}\,\mathrm{d}\lambda, \tag{9}$$

where the Planck function B_λ at wavelength range from λ to $\lambda + \mathrm{d}\lambda$ is given by $B_\lambda = 2hc^2\lambda^{-5}[\exp(hc/\lambda k_{\mathrm{B}}T) - 1]^{-1}$, where h and k_{B} are the Planck and Boltzmann constants. It is well-known that the Planck function exhibits a maximum at a wavelength λ_{eff} that fulfills the condition $\lambda_{\mathrm{eff}}T = 2897.9\ \mu\mathrm{m\,K}$. We consider the temperature range of $T = 2000$–$12000\ \mathrm{K}$, which corresponds to the wavelength range of $\lambda_{\mathrm{eff}} = 0.24$–$1.45\ \mu\mathrm{m}$. Since the peak of the Planck function occurs in a very narrow wavelength range centered at λ_{eff}, we may perform the integration of Eq. (9) over the wavelength range from 0.14 to 300 μm, instead of 0 to ∞, for the practical computation.

2.6. Configuration and polarizability of dipoles

We model fluffy aggregates by a ballistic particle–cluster aggregate (BPCA) and a ballistic cluster–cluster aggregate (BCCA). The BPCA and BCCA have been produced by three-dimensional computer simulations based on the assumption that the sticking probabilities are unity.[53] The individual monomers forming the aggregates are assumed to be compact spheres identical in size and material composition. If the radius r_{m} of the spherical monomer is larger than the wavelength of the incident radiation, the monomers must be divided into pieces small compared with the wavelength to apply the DDA. It is worth noting that computational results performed by the DDA depend on the choice of dipole polarizabilities. When a particle is divided into cubic cells, the lattice dispersion relation (LDR) method may yield the most accurate results among several methods for determining the dipole polarizabilities.[46,47] However, the great number of dipoles requires a huge computational memory and cpu time to perform the DDA. On the other hand, if the size parameter $X_{\mathrm{m}} \equiv kr_{\mathrm{m}}$ of the monomer is small enough to replace the monomers by single dipoles, we can reduce the computational requirement. Recently, it has been shown that the a1-term method proposed by Okamoto[48,49] is superior to the LDR method for a cluster of spherical monomers replaced by single dipoles and can yield reasonable results for $X_{\mathrm{m}} \leq 1$.[50] Accordingly, we assume that the radius of the constituent monomer is $r_{\mathrm{m}} = 0.01\ \mu\mathrm{m}$, which yields $X_{\mathrm{m}} \leq 0.45$ for the wavelength of $\lambda = 0.14$–$300\ \mu\mathrm{m}$, so that the a1-term method is applicable to determine the dipole polarizabilities of the spherical monomers.

Furthermore, the accuracy of the a1-term method may increase when a randomly orientated average is considered in the computations.[48] The orientation of an aggregate can be specified by the Euler angles (ϕ, θ, ψ). We consider n_ϕ values of ϕ, n_θ values of θ, and n_ψ values of ψ to estimate the orientational averages and select the Euler angles (ϕ, θ, ψ) so that ϕ, $\cos\theta$, and ψ are uniformly distributed in the range of $0 \leqq \phi < 360^\circ$, $-1 \leq \cos\theta \leq 1$, and $0 \leq \psi < 360^\circ$, respectively. Computer resources restricts the evaluation of the average quantities by $(n_\phi, n_\theta, n_\psi) = (7, 7, 7)$ orientations, i.e., by a total of 343 different orientations.

The size of the aggregates can be characterized by the radius r_{V} of the volume-equivalent sphere. For homogeneous spherical particles exposed to blackbody radiation, it is well-known that the radiation pressure force per mass of the particle is maximized when the size parameter $X_{\mathrm{eff}} \equiv k_{\mathrm{eff}}r_{\mathrm{V}}$ of the particle is approximately unity, where $k_{\mathrm{eff}} = 2\pi/\lambda_{\mathrm{eff}}$. We shall therefore determine the radius r_{V} of the aggregates so that the size parameter X_{eff} of the aggregates is close to unity. Hence we deal with the aggregates composed of 256 monomers that have the volume-equivalent radius of $r_{\mathrm{V}} = 0.0635\ \mu\mathrm{m}$, because the size parameter of the aggregates having radius $r_{\mathrm{V}} = 0.0635\ \mu\mathrm{m}$ is

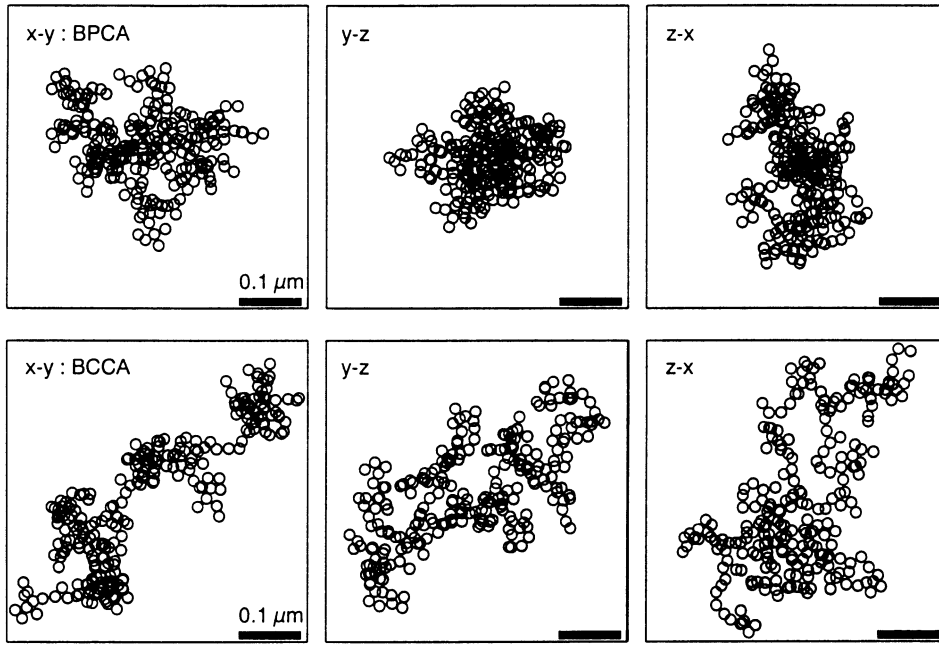

Fig. 1. The projection of aggregates onto the x–y (left), y–z (center), and z–x (right) planes. Upper panel: the ballistic particle–cluster aggregate (BPCA); lower panel: ballistic cluster–cluster aggregate (BCCA). The thick line at the right bottom corner in the each panel indicates the length of 0.1 μm.

$X_{\text{eff}} = 0.275$–1.65 for the wavelength $\lambda_{\text{eff}} = 0.24$–$1.45$ μm. On the other hand, the size parameter X_{V} of the aggregates for the wavelength of $\lambda = 0.14$–300 μm ranges from 0.00133 to 2.85.

The projections of the BPCA and BCCA onto x–y, y–z, and z–x planes in the arbitrary coordinate system are shown in Fig. 1. The length of the thick bar given in the right bottom of each panel corresponds to 0.1 μm. Compared with the BCCA, the BPCA is relatively compact structure and therefore the porosity of the BPCA is lower than that of the BCCA. Note that the constituent monomers, in other words, dipoles are not located on any periodic lattice. We consider two kinds of material composition for aggregates, i.e., silicate and carbon as representatives of dielectric and absorbing material, respectively. The complex refractive index for silicate is taken from the data of astronomical silicate of Laor and Draine[51] and that for carbon from the data of amorphous carbon (AC1) of Rouleau and Martin.[52]

3. NUMERICAL RESULTS

3.1. Cross sections of extinction and scattering

Figure 2 shows the cross sections of extinction C_{ext} and scattering C_{sca} for silicate (left panel) and carbon (right panel) particles having radius $r_{\text{V}} = 0.0635$ μm as a function of wavelength λ. The solid and dashed lines indicate the cross sections for the aggregates and spheres, respectively. The cross sections for the BPCA and the BCCA are separately displayed in the upper and lower panels of Fig. 2.

The dependence of the extinction and scattering cross sections on wavelength reflects the material composition of the particles rather than the shape and structure of the particles, although the cross sections for the aggregates are different from those for the spheres. When the size parameter of the particle is much less than unity ($X_{\text{V}} \ll 1$), the C_{ext} and C_{sca} for the aggregates are similar to, but slightly larger than those for the volume-equivalent spheres. On the other hand, if the size parameter is approximately unity ($X_{\text{V}} \approx 1$), the cross sections for the aggregates are smaller than those for the spheres. At larger size parameter ($X_{\text{V}} \geq 2.5$), however, the cross sections for the aggregates can exceed those for the spheres.

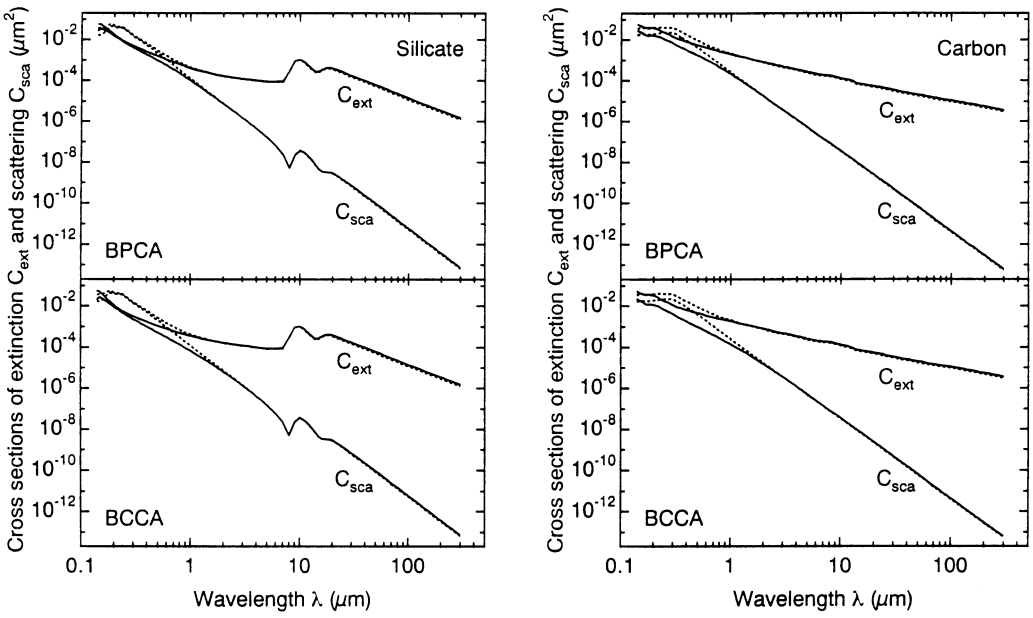

Fig. 2. Cross sections of extinction C_{ext} and scattering C_{sca} for the fluffy aggregates (solid line) and the spheres (dotted line) as a function of wavelength λ ranging from 0.14 to 300 μm. Left top: silicate BPCA; left bottom: silicate BCCA; right top: carbon BPCA; right bottom: carbon BCCA. The cross sections are averaged over 343 different orientations.

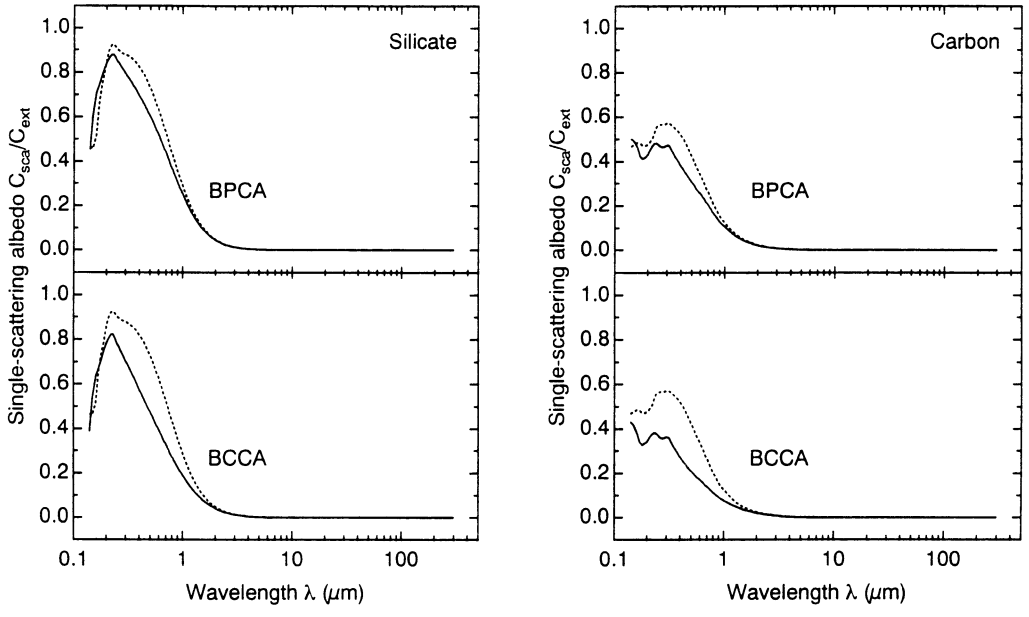

Fig. 3. Single-scattering albedo $\bar{\omega}_0$ for the fluffy aggregates (solid line) and the spheres (dotted line). See also Fig. 2.

The ratio of the scattering cross section C_{sca} to the extinction cross section C_{ext} defines the single-scattering albedo of the particle. Figure 3 displays the single-scattering albedo for silicate (left panel) and carbon (right panel) particles versus wavelength. The single-scattering albedos for the BPCA and the BCCA are shown in the upper and lower panels, respectively, of Fig. 3 (solid lines). The albedo for the spheres identical in the volume and material is appended in Fig. 3 (dotted line) for comparison.

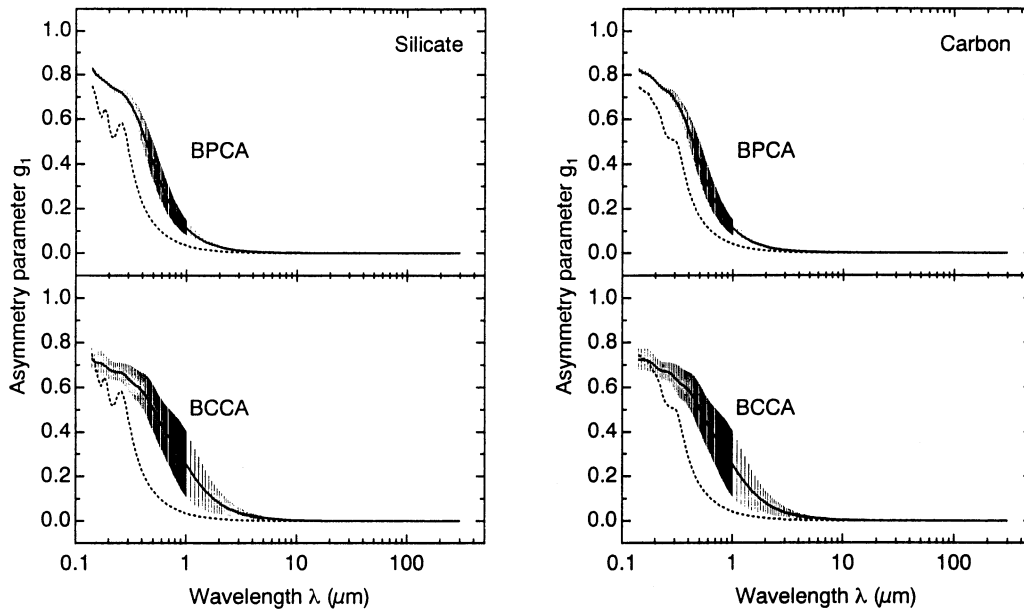

Fig. 4. Asymmetry parameter g_1 parallel to the wave vector $\boldsymbol{k}$. See also Fig. 2.

The single-scattering albedo for the particle increases with decreasing wavelength, accompanied with a sudden drop at very short wavelength. The albedo for the aggregate shows the maximum at $X_V \cong 1.7$ ($\lambda \cong 0.23$ μm) for different morphology and material, although carbon aggregates possess an additional maximum of the albedo at $X_V \cong 1.3$ ($\lambda \cong 0.3$ μm). On the other hand, the single-scattering albedo for the spheres achieves its maximum at $X_V \approx 1.7$ for silicate spheres and at $X_V \approx 1.3$ for carbon spheres.

Although the wavelength dependence of the albedo for the aggregate is similar to that for the sphere, the magnitude of the albedo at a certain wavelength depends on the morphology of the particle. The albedo of the aggregate tends to be lower than that for the volume-equivalent sphere at $X_V \leq 1$. At larger size parameter $X_V \gg 1$, however, the albedo of the aggregate can be higher than that for the sphere. Compared with the BCCA, the BPCA has larger value of the single-scattering albedo, independent of the constituent material. Consequently, the wavelength dependence of the albedo for fluffy aggregates tends to be weaker than that for homogeneous spheres.

The magnitude of the single-scattering albedo depends on the constituent material of the particles rather than the shape and structure in the size parameter range of $X_V \leq 1$. The albedo for the silicate aggregates can be greater than 0.5 at $X_V \leq 1$, because the scattering by the silicate aggregates dominates the absorption in this range of the size parameter. On the other hand, the albedo for the carbon aggregates is less than 0.5 at the whole wavelength range as a consequence of the absorbing character.

3.2. Asymmetry parameter

Figure 4 shows the parallel component of the asymmetry parameter g_1 for silicate (left panel) and carbon (right panel) particles versus the wavelength of incident light. The asymmetry parameters g_1 for aggregates and spheres are distinguished by solid and dotted lines, respectively. The upper panel in Fig. 4 displays the g_1 for the BPCA and the lower panel the g_1 for the BCCA. The vertical bars denote the standard deviation from the orientational-average value of the asymmetry parameter g_1, caused by the dependence of the quantity on the particle orientation.

Although the wavelength dependence of the asymmetry parameter g_1 for the spherical particles oscillates at larger size parameter ($X_V > 1$), the g_1 for the aggregates smoothly increases with increasing size parameter X_V of the aggregates. As a result, the wavelength dependence of the g_1 for the aggregates becomes similar for different material of the aggregates.

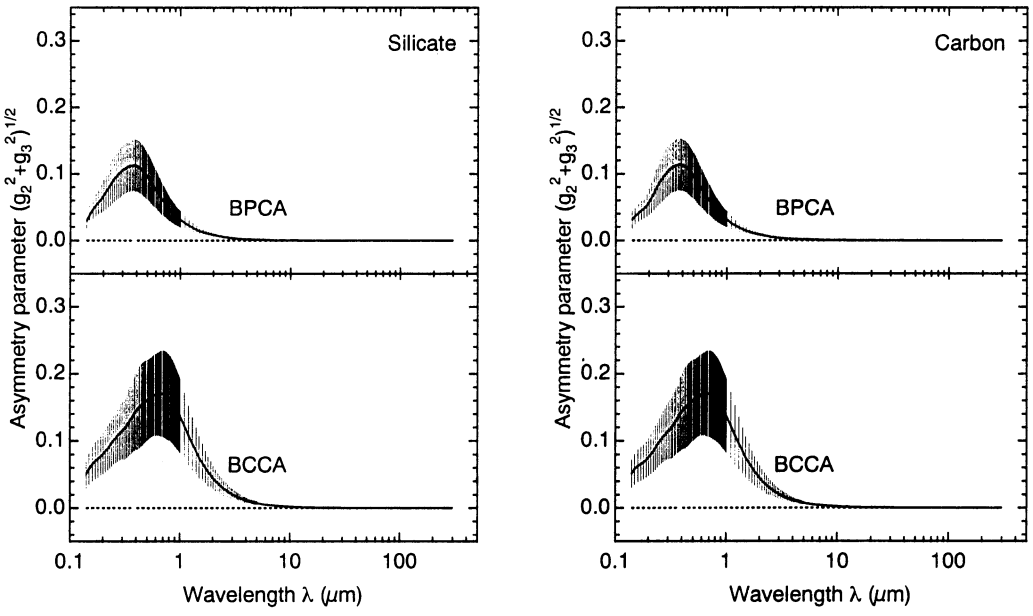

Fig. 5. The asymmetry parameter $(g_2^2 + g_3^2)^{1/2}$ perpendicular to the wave vector $\boldsymbol{k}$. See also Fig. 2.

The dependence of the g_1 on the wavelength varies with the shape and structure of the aggregates. The asymmetry parameter g_1 for the BPCA is higher than that for the BCCA at $X_V \gg 1$, but lower at $X_V \leq 1$. In the wavelength range considered in this paper, the asymmetry parameter g_1 for the BPCA is higher than that for spheres, irrespective of the constituent material. Compared with the spheres, the g_1 for the BCCA similarly shows a higher value, except for the shortest wavelength range. Clearly, the dependence of the g_1 on the particle orientation is stronger for the BCCA than for the BPCA.

The component of the asymmetry parameter perpendicular to the wave vector $\boldsymbol{k}$ is shown in Fig. 5. We estimate the perpendicular component of the asymmetry parameter by $\sqrt{g_2^2 + g_3^2}$, instead of either g_2 or g_3, because $\hat{\boldsymbol{e}}_2$ and $\hat{\boldsymbol{e}}_3$ are arbitrary and the g_2 and g_3 disappear on the orientational average. The left and right panels illustrate the asymmetry parameter $\sqrt{g_2^2 + g_3^2}$ for silicate and carbon particles, respectively. The asymmetry parameters $\sqrt{g_2^2 + g_3^2}$ for the BPCA and the BCCA are separately shown in the upper and lower panels of Fig. 5. The vertical bars indicate the standard deviation of the $\sqrt{g_2^2 + g_3^2}$ after averaging by 343 orientations.

The asymmetry parameter $\sqrt{g_2^2 + g_3^2}$ for the silicate aggregates is similar to that for the carbon aggregates, although the morphology of the aggregates influences differently on the wavelength dependence of the asymmetry parameter. The perpendicular component of the asymmetry parameter $\sqrt{g_2^2 + g_3^2}$ for the BCCA exceeds that for the BPCA in the whole range of wavelength. The asymmetry parameter $\sqrt{g_2^2 + g_3^2}$ shows the maximum occurring at $X_V = 1.1$ ($\lambda = 0.37$ μm) for the BPCA and at $X_V = 0.6$ ($\lambda = 0.665$ μm) for the BCCA.

3.3. Radiation pressure cross section

The cross section C_{pr} of radiation pressure for silicate and carbon aggregates is shown separately in the left and right panels of Fig. 6 as solid lines. For comparison, the radiation pressure cross section for the volume-equivalent sphere is included in Fig. 6 as a dotted line. The upper and lower panels illustrate the C_{pr} for the BPCA and the BCCA, respectively. The parallel and perpendicular components of the C_{pr} are indicated by $C_{pr,1}$ and $\sqrt{C_{pr,2}^2 + C_{pr,3}^2}$, respectively.

When the size parameter of the aggregates is $0.3 \leq X_V \leq 2$, the parallel component of radiation pressure cross section $C_{pr,1}$ for the aggregates is smaller than that for the volume-equivalent spheres. Furthermore, the value of the radiation pressure cross section $C_{pr,1}$ for the BCCA is slightly less than

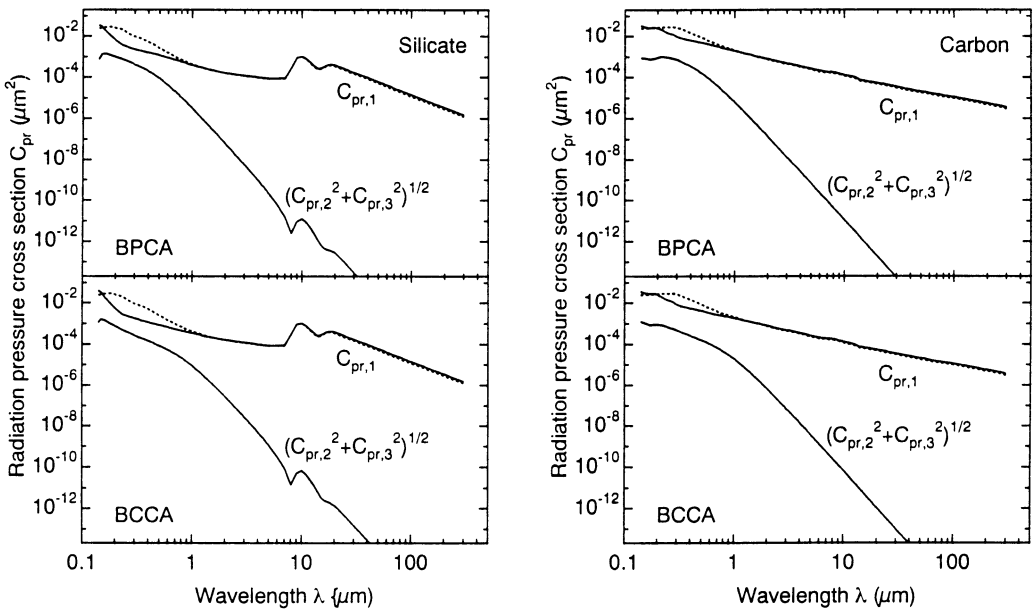

Fig. 6. The parallel $C_{\mathrm{pr},1}$ and perpendicular $(C_{\mathrm{pr},2}^2 + C_{\mathrm{pr},3}^2)^{1/2}$ components of radiation pressure cross section with respect to the wave vector $\boldsymbol{k}$. See also Fig. 2.

that for the BPCA at the size parameter of $0.1 \leq X_{\mathrm{V}} \leq 1.8$. However, the $C_{\mathrm{pr},1}$ for the aggregates can exceed that for the spherical particles at larger size parameter of $X_{\mathrm{V}} > 2$. Moreover, the aggregates have slightly larger cross section $C_{\mathrm{pr},1}$ of radiation pressure at smaller size parameter $X_{\mathrm{V}} \ll 1$, compared with the volume-equivalent spheres.

On the other hand, the radiation pressure cross section $\sqrt{C_{\mathrm{pr},2}^2 + C_{\mathrm{pr},3}^2}$ perpendicular to the incident radiation decreases markedly with increasing wavelength. Note that for homogeneous spherical particles $\sqrt{C_{\mathrm{pr},2}^2 + C_{\mathrm{pr},3}^2}$ is nonexistent. The perpendicular component of the radiation pressure cross section for the BCCA exceeds that for the BPCA at $X_{\mathrm{V}} \ll 1$, but becomes smaller at $X_{\mathrm{V}} \approx 1$. Clearly, the dependence of the $\sqrt{C_{\mathrm{pr},2}^2 + C_{\mathrm{pr},3}^2}$ on the constituent material originates from the scattering cross section, because the asymmetry parameter for the aggregates is mostly independent of the material composition.

Figure 7 shows the ratio of perpendicular $\sqrt{C_{\mathrm{pr},2}^2 + C_{\mathrm{pr},3}^2}$ to parallel $C_{\mathrm{pr},1}$ cross sections for the silicate (left panel) and carbon (right panel) particles. The ratios for the BPCA and the BCCA are separately illustrated in the upper and lower panels of Fig. 7 as solid lines. Although the ratio for homogeneous spherical particles is included in Fig. 7 as dotted line, the value lies exactly on zero because of the symmetrical shape.

The ratio of the radiation pressure cross sections achieves its maximum at $X_{\mathrm{V}} \cong 1.7$ ($\lambda \cong 0.24$ μm) for the silicate aggregates and at $X_{\mathrm{V}} \cong 1.3$ ($\lambda \cong 0.3$ μm) for the carbon aggregates. The perpendicular components of radiation pressure cross section for the silicate aggregates reach 21 and 17 % of the parallel components for the BPCA and the BCCA, respectively. In contrast to the silicate aggregates, the perpendicular components for carbon BPCA and BCCA are only 7 and 6% of the parallel component at the maximum. The perpendicular component of the radiation pressure cross section relative to the parallel component is negligible for the particles at the size parameter range of $X_{\mathrm{V}} \ll 1$.

When the size parameter of the aggregates exceeds unity ($X_{\mathrm{V}} > 1$), the ratio of the radiation pressure cross sections for the BCCA is less than that for the BPCA. On the other hand, the ratio of the cross sections for the BCCA exceeds that for the BPCA at the size parameter of $X_{\mathrm{V}} < 1$.

3.4. Planck-mean radiation pressure cross section

We notice that the shortest wavelength, $\lambda = 0.14$ μm, adopted in this study may diminish the accuracy of the integration especially at higher temperature T, because $\lambda = 0.14$ μm is situated close

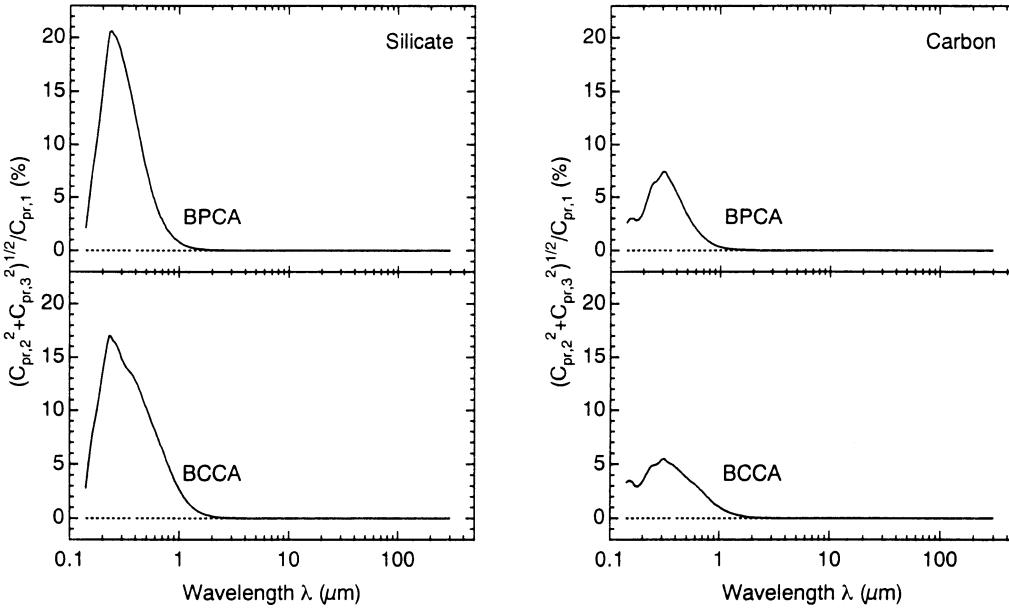

Fig. 7. The ratio of radiation pressure cross sections $(C_{\mathrm{pr},2}^2 + C_{\mathrm{pr},3}^2)^{1/2}/C_{\mathrm{pr},1}$. See also Fig. 2.

to the wavelength λ_{eff} of the maximum B_λ at high temperature. In order to estimate the error in the computation, we compare $\langle C_{\mathrm{pr},1}\rangle$ for spheres integrated over $\lambda = 0.14$–$300\ \mu\mathrm{m}$ with that over $\lambda = 0.001$–$300\ \mu\mathrm{m}$. The relative error of the $\langle C_{\mathrm{pr},1}\rangle$ for silicate and carbon spheres having radius of $0.0635\ \mu\mathrm{m}$ are less than 3.3 and 0.8%, respectively. When the blackbody temperature is below 9000 K ($\lambda_{\mathrm{eff}} = 0.322\ \mu\mathrm{m}$), numerical calculation of the Planck-mean radiation pressure cross section for spheres is accurate within the relative error of 1%. Simply we expect that the Planck-mean cross section of radiation pressure for fluffy aggregates can be obtained within the similar accuracy.

Figure 8 illustrates the Planck-mean cross section of radiation pressure for silicate (left panel) and carbon (right panel) particles having the identical radius $r_{\mathrm{V}} = 0.0635\ \mu\mathrm{m}$ as a function of blackbody temperature T. The Planck-mean radiation pressure cross sections $\langle C_{\mathrm{pr}}\rangle$ for the BPCA, BCCA, and spheres are indicated by open triangles, squares, and circles, respectively. While the parallel component of the Planck-mean radiation pressure cross section is denoted as $\langle C_{\mathrm{pr},1}\rangle$, the perpendicular component is estimated by $\sqrt{\langle C_{\mathrm{pr},2}\rangle^2 + \langle C_{\mathrm{pr},3}\rangle^2}$.

The parallel components $\langle C_{\mathrm{pr},1}\rangle$ of the radiation pressure cross section for the aggregates are lower than those for the volume-equivalent spheres. Furthermore, the $\langle C_{\mathrm{pr},1}\rangle$ for the BPCA is higher than that for the BCCA regardless of the constituent material, although the difference of the $\langle C_{\mathrm{pr},1}\rangle$ between the BPCA and the BCCA is not significant. The carbon aggregates have large cross section of radiation pressure, compared with silicate aggregates in the whole temperature range.

As the temperature T decreases, the $\langle C_{\mathrm{pr}}\rangle$ for the aggregates approaches that of the spheres. Note that homogeneous spherical particles have only the parallel component of the Planck-mean radiation pressure cross section. Consequently, the perpendicular component of the Planck-mean radiation pressure cross section $\sqrt{\langle C_{\mathrm{pr},2}\rangle^2 + \langle C_{\mathrm{pr},3}\rangle^2}$ for the aggregates becomes zero in the limit of $T \to 0$. At lower temperatures, the perpendicular component of the $\langle C_{\mathrm{pr}}\rangle$ for the BCCA exceeds that for the BPCA, irrespective of the material composition.

On the other hand, the cross section of the perpendicular radiation pressure increases with increasing temperature. The perpendicular component of the $\langle C_{\mathrm{pr}}\rangle$ for the BPCA is greater than that for the BCCA when the blackbody temperature rises above $T = 4500$ K ($\lambda_{\mathrm{eff}} = 0.644\ \mu\mathrm{m}$). The perpendicular component of the Planck-mean radiation pressure cross section attains about 10 and 5% for silicate and carbon aggregates, respectively, with respect to the parallel component of the cross section.

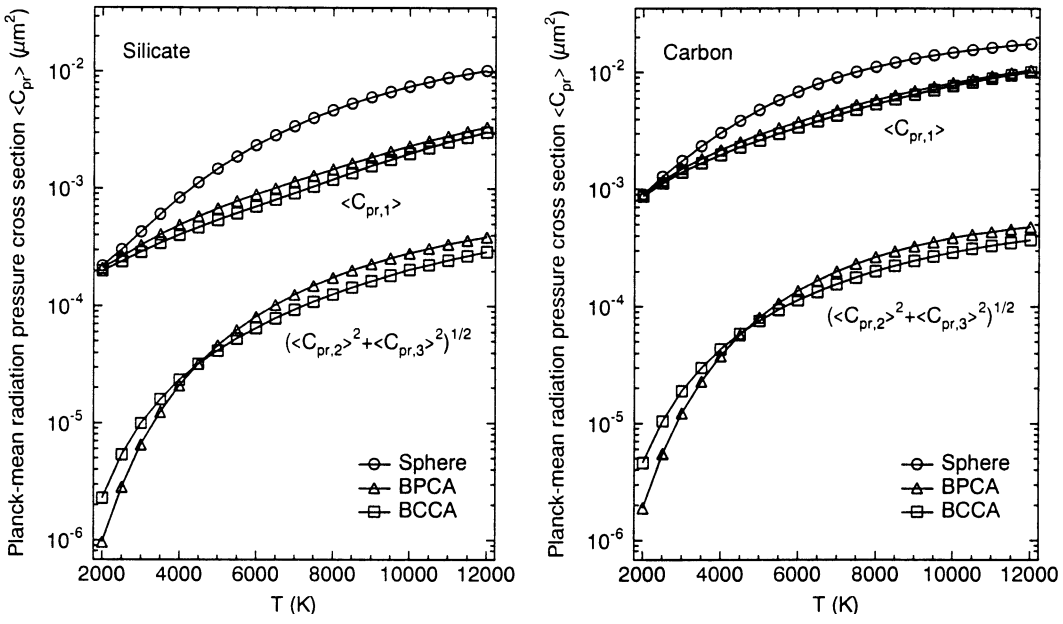

Fig. 8. Planck-mean radiation pressure cross section for BPCA and BCCA compared with that for volume-equivalent sphere, as a function of blackbody temperature T. See also Fig. 2.

4. DISCUSSION

4.1. Asymmetry of light scattering

The perpendicular component of radiation pressure force acting on fluffy aggregates results from the asymmetry of light scattering by the aggregates with respect to the direction of incident radiation. The asymmetry of the scattered light by the aggregates can be described by the asymmetry parameter $\boldsymbol{g}$ defined by Eq. (3). While we have considered the case that the volume-equivalent radius for the BCCA is identical to that for the BPCA, the fluffiness and porosity for the BCCA are higher than those for the BPCA (see Fig. 1). Compared with the BPCA, therefore, the BCCA reveals higher irregularity in the particle morphology, in other words, highly asymmetrical shape and structure. Consequently, a different orientation of the BCCA strongly changes the optical properties, such as the asymmetry parameter $\boldsymbol{g}$, that can be seen in Figs. 4 and 5 as vertical bars.

On the other hand, the perpendicular component of the asymmetry parameter for the BCCA shows a maximum at longer wavelength, compared with the BPCA (see Fig. 5). At longer wavelength, therefore, the BCCA attains a relatively large cross section of radiation pressure perpendicular to the direction of incident wave (see Figs. 6 and 7). Since the long wavelength corresponds to a low temperature of the blackbody radiation, the asymmetry of light scattering by the BCCA becomes effective at low temperatures. In fact, the perpendicular component of the radiation pressure acting on the BCCA exceeds that for the BPCA at lower temperatures (see Fig. 8). These results can be explained by the fact that the geometrical cross section and the radius of gyration for the BCCA are larger than those for the BPCA.[53,54] Namely, the size of the aggregates corresponding to the wavelength of the maximum asymmetry can be characterized by the area-equivalent radius or the radius of gyration, rather than the volume-equivalent radius of the aggregates. It is, therefore, reasonable to conclude that the BCCA behaves like a larger particle than the BPCA and that a large fluctuation in the asymmetry parameter for different orientation of the BCCA arises from a high degree of irregularity of its morphology.

4.2. Single-scattering albedo

The perpendicular component of the radiation pressure force is related to the single-scattering albedo as well as the asymmetry parameter. The single-scattering albedo for silicate aggregates is

higher than that for carbon aggregates (see Fig. 3) and silicate aggregates show also high ratios $\sqrt{C_{\mathrm{pr},2}^2 + C_{\mathrm{pr},3}^2}/C_{\mathrm{pr},1}$ of radiation pressure cross sections, compared with carbon aggregates (see Fig. 7). Accordingly, the perpendicular component of radiation pressure becomes relatively important for silicate aggregates than for carbon aggregates (see Fig. 8). On the other hand, the ratio $\sqrt{C_{\mathrm{pr},2}^2 + C_{\mathrm{pr},3}^2}/C_{\mathrm{pr},1}$ of the radiation pressure cross section can be expressed as $\bar{\omega}_0\sqrt{g_2^2 + g_3^2}/(1 - \bar{\omega}_0 g_1)$, using the albedo $\bar{\omega}_0$. If the asymmetry parameter is unchanged, this function monotonically increases with increasing albedo. Since the asymmetry parameter is almost independent of the constituent material (see Figs. 4 and 5), the material composition of high albedo tends to increase the relative importance of the radiation pressure perpendicular to the direction of incident wave.

It is worth noting that the single-scattering albedo depends not only on the constituent material of the aggregates but also on the aggregate morphology. Hage and Greenberg[55] have concluded that the albedo for absorbing aggregates with $X_{\mathrm{V}} = 1.9 - 10$ decreases with increasing porosity of aggregates. Since the porosity is smaller for the BPCA than for the BCCA (see Fig. 1), the albedo for the BPCA is higher than that of the BCCA (see Fig. 3). In contrast with material composition of the aggregates, the shape and structure of the aggregates influences both the albedo and the asymmetry parameter. Irrespective of the higher albedo for the BPCA, therefore, the perpendicular component of radiation pressure cross section with respect to the parallel component is not always higher for the BPCA than for the BCCA.

4.3. Radiation pressure acting on randomly rotating aggregates

Although the perpendicular component of radiation pressure on the aggregates depends on the asymmetry parameter and the single-scattering albedo, the asymmetry of light scattering perpendicular to the direction of incident radiation disappears for randomly rotating aggregates on the average. Accordingly, the incident radiation exerts a force on the randomly rotating aggregates only in the direction of the incident wave. The radiation pressure acting on the randomly rotating aggregates can be evaluated by the Planck-mean radiation pressure cross section parallel to the incident radiation. Since the Planck function has a very narrow peak at the effective wavelength λ_{eff}, the parallel component of the Planck-mean radiation pressure cross section is mainly determined by the radiation pressure cross section around λ_{eff}. On the other hand, the parallel component of the radiation pressure cross section shows a similar dependence of the extinction cross section on wavelength. In comparison with spheres, low values of extinction cross section for aggregate particles with $1 \leqq X_{\mathrm{V}} \leq 3$ have been derived by West.[34] This result is consistent with that in Fig. 2. In consequence of the low extinction cross sections for the aggregates, the parallel component of the radiation pressure cross section for the aggregates around λ_{eff} results in smaller values, compared with the sphere (see Fig. 6). Consequently, the Planck-mean radiation pressure cross section parallel to the direction of incident radiation is smaller for the aggregates than for the sphere. Therefore, when $X_{\mathrm{eff}} \simeq 1$, the radiation pressure acting on randomly rotating aggregates is weaker than that acting on the volume-equivalent spheres. This coincides with the results obtained by Mie theory combined with the effective medium theory.[5,29] Since radiation pressure per mass of the particle exerted in the direction of incident radiation is maximized at $X_{\mathrm{eff}} \simeq 1$, we conclude that the maximum radiation pressure per mass of the particle is diminished for fluffy aggregates.

Acknowledgements—We thank John F. James and James F. McKenzie for improving the manuscript, Hajime Okamoto for instruction of the a1-term method and Youhei Kitada for providing the coordinate data of the ballistic particle–cluster aggregate and the ballistic cluster–cluster aggregate. We also thank the anonymous referees for their useful comments. We are grateful to Drs. B. T. Draine and P. Flatau for providing the original Fortran program of the discrete dipole approximation.

REFERENCES

1. Ishimoto, H., Mukai, T., Kimura, H. and Maruyama, K., Orbital evolution of the porous particles from comets and asteroids. In *Meteoroids and their Parent Bodies*, eds J. Štohl and I. P. Williams, Astronomical Institute of the Slovak Academy of Sciences, Bratislava, 1993, pp. 65–68.
2. Robertson, H. P., Dynamical effects of radiation in the solar system. *Monthly Notices of the Royal Astronomical Society*, 1937, **97,** 423–438.

3. Wyatt Jr, S. P. and Whipple, F. L., The Poynting-Robertson effect on meteor orbits. *Astrophys. J*., 1950, **111,** 134–141.
4. Voshchinnikov, N. V. and Il'in, V. B., Dust sweeping by the radiation of different types of stars. *Soviet Astronomy*, 1983, **27,** 650–654.
5. Kimura, H., Ishimoto, H. and Mukai, T., A study on solar dust ring formation based on fractal dust models. *Astronomy Astrophys*., 1997, **326,** 263–270.
6. Grün, E., Gustafson, B., Mann, I., Baguhl, M., Morfill, G. E., Staubach., P., Taylor, A. and Zook, H. A., Interstellar dust in the heliosphere. *Astronomy Astrophys*., 1994, **286,** 915–924.
7. Artymowicz, P., Modeling and understanding the dust around Beta Pictoris. In *Circumstellar Dust Disks and Planet Formation*, eds. R. Ferlet and A. Vidal-Madjar. Editions Frontieres, Singapore, 1994, pp. 47–65.
8. Artymowicz, P. and Clampin, M., Dust around main-sequence stars: nature or nurture by the interstellar medium? *Astrophys. J*., 1997, **490,** 863–878.
9. Rannou, P., Cabane, M., Chassefiere, E., Botet, R., McKay, C. P. and Courtin, R., Titan's geometric albedo: role of the fractal structure of the aerosols. *Icarus*, 1995, **118,** 355–372.
10. Krivova, N. A. and Il'in, V. B., Dust shells around Herbig Ae/Be stars with Algol-like minima: modeling of photometric observations. *Astronomy Lett*., 1997, **23,** 791–798.
11. van de Hulst, H. C., *Light Scattering by Small Particles*. Dover, New York, 1957.
12. Bohren, C. F. and Huffman, D. R., *Absorption and Scattering of Light by Small Particles*. Wiley-Interscience, New York, 1983.
13. Waterman, P. C., Matrix formulation of electromagnetic scattering. *Proc. IEEE*, 1965, **53,** 805–812.
14. Waterman, P. C., Symmetry, unitarity, and geometry in electromagnetic scattering. *Phys. Rev. D*, 1971, **3,** 825–839.
15. Mishchenko, M. I., Radiation pressure on randomly-oriented nonspherical particles. *Astrophys. Space Sci*., 1991, **180,** 163–169.
16. Asano, S. and Yamamoto, G., Light scattering by a spheroidal particle. *Appl. Opt*., 1975, **14,** 29–49.
17. Cohen, A. and Alpert, P., Radiation pressure on randomly oriented infinite cylinders. *Appl. Opt*., 1980, **19,** 558–560.
18. Voshchinnikov, N. V. and Il'in, V. B., Radiation pressure on cylindrical particles. *Opt. Spectrosc*. (*USSR*), 1983, **55,** 304–306.
19. Voshchinnikov, N. V., Radiation pressure on spheroidal particles. *Sov. Astronomy*, 1990, **34,** 429–432.
20. Voshchinnikov, N. V. and Farafonov, V. G., Optical properties of spheroidal particles. *Astrophys. Space Sci*., 1993, **204,** 19–86.
21. Il'in, V. B. and Voshchinnikov, N. V., Radiation pressure on non-spherical dust grains in envelopes of late-type giants. *Astronomy Astrophys. Suppl. Ser*., 1998, **128,** 187–196.
22. Dobbins, R. A. and Megaridis, C. M., Morphology of flame-generated soot as determined by thermophoretic sampling. *Langmuir*, 1987, **3,** 254–259.
23. Bar-Nun, A., Kleinfeld, I. and Ganor, E., Shape and optical properties of aerosols formed by photolysis of acetylene, ethylene, and hydrogen cyanide. *J. Geophys. Res*., 1988, **93,** 8383–8387.
24. Brownlee, D. E., Tomandl, D. A. and Hodge, P. W., Extraterrestrial particles in the stratosphere. In *Interplanetary Dust and Zodiacal Light*, Lecture Notes in Physics, Vol. 48, eds. H. Elsässer and H. Fechtig. Springer, Berlin, 1976, pp. 279–283.
25. Brownlee, D. E., Microparticle studies by sampling techniques. In *Cosmic Dust*, ed. J. A. M. McDonnell. Wiley-Interscience, New York, 1978, pp. 295–336.
26. Brownlee, D. E., Pilachowski, L., Olszewski, E. and Hodge, P. W., Analysis of interplanetary dust collections. In *Solid Particles in the Solar System*, ed. I. Halliday and B. A. McIntosh. D. Reidel, Dordrecht, 1980, pp. 333–342.
27. Witten, T. A. and Cates, M .E., Tenuous structures from disorderly growth processes. *Science*, 1986, **232,** 1607–1612.
28. Cabane, M., Rannou, P., Chassefière, E. and Israel, G., Fractal aggregates in Titan's atmosphere. *Planetary Space Sci*., 1993, **41,** 257–267.
29. Mukai, T., Ishimoto, H., Kozasa, T., Blum, J. and Greenberg, J. M., Radiation pressure forces of fluffy porous grains. *Astronomy Astrophys*., 1992, **262,** 315–320.
30. Wilck, M. and Mann, I., Radiation pressure forces on "typical" interplanetary dust grains. *Planetary Space Sci*., 1996, **44,** 493–499.
31. Purcell, E. M. and Pennypacker, C. R., Scattering and absorption of light by nonspherical dielectric grains. *Astrophys. J*., 1973, **186,** 705–714.
32. Wright, E. L., Fractal dust grains around R Coronae Borealis stars. *Astrophys. J*., 1989, **346,** L89–L91.
33. Bazell, D. and Dwek, E., The effects of compositional inhomogeneities and fractal dimension on the optical properties of astrophysical dust. *Astrophys. J*., 1990, **360,** 142–150.
34. West, R. A., Optical properties of aggregate particles whose outer diameter is comparable to the wavelength. *Appl. Opt*., 1991, **30,** 5316–5324.
35. Kozasa, T., Blum, J. and Mukai, T., Optical properties of dust aggregates I. Wavelength dependence. *Astronomy Astrophys*., 1992, **263,** 423–432.
36. Kozasa, T., Blum, J., Okamoto, H. and Mukai, T., Optical properties of dust aggregates II. Angular dependence of scattered light. *Astronomy Astrophys*., 1993, **276,** 278–288.

37. Okamoto, H., Mukai, T. and Kozasa, T., The 10 μm feature of aggregates in comets. *Planetary Space Sci*., 1994, **42,** 643–649.
38. Lumme, K. and Rahola, J., Light scattering by porous dust particles in the discrete-dipole approximation. *Astrophys. J*., 1994, **425,** 653–667.
39. Xing, Z. and Hanner, M. S., Modelling the temperature of cometary particles. In *Physics*, *Chemistry*, *and Dynamics of Interplanetary Dust*, Astronomical Society of the Pacific Conference Series, Vol. 104, eds. B. Å. S. Gustafson and M. S. Hanner. Astronomical Society of the Pacific, San Francisco, 1996, pp. 437–441.
40. Lumme, K., Rahola, J. and Hovenier, J. W., Light scattering by dense clusters of spheres. *Icarus*, 1997, **126,** 455–469.
41. Xing, Z. and Hanner, M. S., Light scattering by aggregate particles. *Astronomy Astrophys*., 1997, **324,** 805–820.
42. Levasseur-Regourd, A. C., Cabane, M., Worms, J. C. and Haudebourg, V., Physical properties of dust in the solar system: relevance of a computational approach and of measurements under microgravity conditions. *Adv. Space Res*., 1997, **20,** 1585–1594.
43. Draine, B. T., The discrete-dipole approximation and its application to interstellar graphite grains. *Astrophys. J*., 1988, **333,** 848–872.
44. Draine, B. T. and Flatau, P. J., Discrete-dipole approximation for scattering calculations. *J. Opt. Soc. Amer. A*, 1994, **11,** 1491–1499.
45. Press, W. H., Flannery, B. P., Teukolsky, S. A. and Vetterling, W. T., *Numerical Recipes*. Cambridge University, New York, 1986, pp. 114–115.
46. Draine, B. T. and Goodman, J., Beyond Clausius–Mossotti: wave propagation on a polarizable point lattice and the discrete dipole approximation. *Astrophys. J*., 1993, **405,** 685–697.
47. Flatau, P. J., Fuller, K. A. and Mackowski, D. W., Scattering by two spheres in contact: comparisons between discrete-dipole approximation and modal analysis. *Appl. Opt*., 1993, **32,** 3302–3305.
48. Okamoto, H., Light scattering by clusters: the a1-term method. *Opt. Rev*., 1995, **2,** 407–412.
49. Okamoto, H., Applicability of a1-term method to the scattering by irregularly shaped interplanetary dust grains. In *Physics*, *Chemistry*, *and Dynamics of Interplanetary Dust*, Astronomical Society of the Pacific Conference Series, Vol. 104, eds. B. Å. S. Gustafson and M. S. Hanner. Astronomical Society of the Pacific, San Francisco, 1996, pp. 423–426.
50. Okamoto, H. and Xu, Y., Light scattering by irregular interplanetary dust particles. *Earth Planets Space*, 1998, **50,** in press.
51. Laor, A. and Draine, B. T., Spectroscopic constraints on the properties of dust in active galactic nuclei. *Astrophys. J*., 1993, **402,** 441–468.
52. Rouleau, F. and Martin, P. G., Shape and clustering effects on the optical properties of amorphous carbon. *Astrophys. J*., 1991, **377,** 526–540.
53. Kitada, Y., Nakamura, R. and Mukai, T., Correlation between cross section and surface area of irregularly shaped particle. In *Proceedings of the* 3*rd International Congress on Optical Particle Sizing*, ed. M. Maeda. 1993, pp. 121–125.
54. Weidenschilling, S. J., Donn, B. and Meakin, P., The physics of planetesimal formation. In *The Formation and Evolution of Planetary Systems*, eds. H. A. Weaver and L. Danly. Cambridge University, New York, 1989, pp. 131–150.
55. Hage, J. I. and Greenberg, J. M., A model for the optical properties of porous grains. *Astrophys. J*., 1990, **361,** 251–259.